ACS APPLIED MATERIALS & INTERFACES

Research Article

www.acsami.org

Vapor–Liquid–Solid Growth of One-Dimensional Tin Sulfide (SnS) Nanostructures with Promising Field Emission Behavior

Sachin R. Suryawanshi,[†] Sambhaji S. Warule,[‡] Sandip S. Patil,[§] Kashinath R. Patil,[‡] and Mahendra A. More*[,†]

[†]Centre for Advanced Studies in Materials Science and Condensed Matter Physics, Department of Physics, University of Pune, Ganeshkhind Road, Pune 411007, India

[‡]National Chemical Laboratory (NCL), Council of Scientific and Industrial Research (CSIR), Dr. Homi Bhabha Road, Pune 411008, India

[§]Department of Physics, Modern College of Arts, Science and Commerce, Shivaji Nagar, Pune 411005, India

Supporting Information

ABSTRACT: Single-crystalline ultralong tin sulfide (SnS) nanowires has been grown by a thermal evaporation technique under optimized conditions on gold-coated silicon substrates, and for the first time, field emission investigations on the SnS nanowires at the base pressure of 1×10^{-8} mbar are reported. It has been revealed that the surface morphology of the as-synthesized SnS nanostructures is significantly influenced by the deposition temperature and duration. Structural and morphological analyses of as-synthesized SnS nanostructures have been carried out using X-ray diffraction (XRD), scanning electron microscopy (SEM), and transmission electron microscopy (TEM). To understand the optical and electronic properties of as-synthesized SnS nanowires, ultraviolet–visible (UV–vis), photoluminescence (PL), and X-ray photoelectron spectroscopy (XPS) studies were carried out. The SEM and TEM measurements reveal the formation of ultralong SnS nanowires, with an average diameter of 80 nm. A plausible explanation on the vapor–solid–liquid (VLS) growth mechanism based on the experimental results and reported literature has been presented. Furthermore, the field emission characteristics of the SnS nanowires are found to be superior to the other metal chalcogenide nanostructures. The synthesized SnS nanowire emitter delivers a high current density of ~2.5 mA/cm^2 at an applied electric field of ~4.55 V/μm. The emission current stability over a period of 6 h is observed to be good. The observed results demonstrate the potential of the SnS nanowire emitter as an electron source for practical applications in vacuum nano/microelectronic devices.

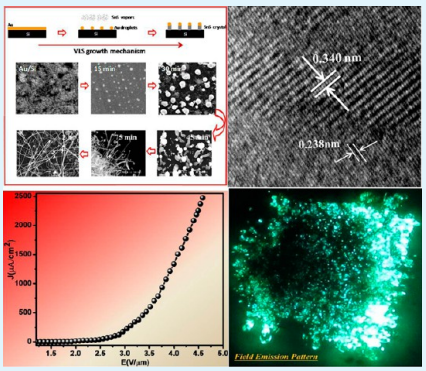

KEYWORDS: *thermal evaporation, 1D nanostructure, SnS nanowires, vapor–liquid–solid (VLS) growth, electron emission*

1. INTRODUCTION

Nanostructures of semiconductor chalcogenides have gained importance in recent years because of tailoring of the dielectric,[1] electric,[2] and optical properties via shape and size control[3] and their potential applications in photonics,[4] optoelectronic,[5] vacuum micro/nanoelectronic devices.[6,7] Amongst the various chalcogenides, tin sulfide (SnS) is a IV–VI group direct narrow band gap semiconductor ($E_g \sim 1.30$ eV, at 300 K). Furthermore, it exhibits both the p- and n-type conduction.[8] Normally, SnS has an orthorhombic structure composed of double layers of tightly bound Sn–S atoms, with weak intralayer bonding of van der Waal's type.[9]

With the advent of nanotechnology, various researchers have reported synthesis of different nanoforms of SnS, such as nanowires,[8] nanoribbons,[10] nanobelts,[11] and nanotubes.[12] In this context, Yue et al. have synthesized single-crystalline SnS nanowire arrays using an anodic aluminum oxide (AAO) template-assisted pulsed electrochemical route.[8] Hydrothermal synthesis of flexible SnS nanobelts for lithium ion battery applications has been reported by Lu et al.[11] Recently, solution-based synthesis of ultrathin single-crystalline SnS nanoribbons has been attempted for photodetector applications.[10] Radovsky et al. have synthesized SnS_2 and SnS_2/SnS nanotubes under a controlled environment.[12] Photocatalytic and photo-electrochemical properties of porous SnS_x (x = 1 and 2) architectures have been reported by Chao et al.[13] The authors have used a template-free polyol refluxing route to build the SnS structures. Despite SnS being a potential candidate for applications in nano-optoelectronic devices, the literature survey reveals that reports on the synthesis of SnS nanostructures are sparse in contrast to other chalcogenides and there is scope to explore a facile route toward synthesis of SnS nanostructures. Thermal evaporation of precursor(s) in a quartz tube furnace under a controlled environment is one of the widely employed methods

Received: November 13, 2013
Accepted: January 16, 2014
Published: January 16, 2014

 © 2014 American Chemical Society

for synthesis of a variety of nanostructures. Although synthesis of SnS nanowires by thermal evaporation is reported by Yue et al., the authors have used two separate sources of SnS and S powders, which were evaporated at 800 and 150 °C, respectively. Furthermore, a small amount of hydrogen was mixed [flow rate of ∼10 standard cubic centimeters per minute (sccm)] with the carrier gas, argon (flow rate of ∼200 sccm). This synthesis protocol appears to be tedious, because controlling the vaporization temperatures (i.e., vapor pressures) of the individual sources and handling hydrogen gas at high temperatures involve complexity.[8]

Herein, we report synthesis of single-crystalline ultralong SnS nanowires using a facile thermal evaporation route. Because the one-dimensional (ID) nanostructures owing to their high aspect ratio are favorable for cold cathode applications, field emission (FE) studies of the as-synthesized SnS nanowires have been carried out and observed to be superior to the other chalcogenide nanostructures. The FE studies of SnS nanowires reported herein are the first of their kind, and to the best of our knowledge, there are no such reports found in the literature.

2. EXPERIMENTAL SECTION

2.1. Synthesis of SnS Nanowires. In the present studies, single-crystalline SnS nanowires were synthesized using a facile thermal evaporation route. In a typical synthesis experiment, an alumina boat filled with an appropriate amount of high-purity SnS_2 powder was placed in the middle of a programmable quartz tube furnace. A pre-cleaned gold (Au)-coated silicon (Si) substrate (1.0 × 1.0 cm) was kept above the alumina boat upstream of the gas flow. For substrate preparation, pieces of silicon were first ultrasonically cleaned in ethanol and acetone, followed by drying under nitrogen gas. These cleaned substrates were immediately mounted in a direct current (DC) sputter coater, wherein a very thin layer of Au (∼40 Å) was deposited. The quartz tube furnace was flushed with argon (Ar), at a flow rate of 100 sccm for 1 h. The furnace temperature was raised to 800 °C at a rate of 20°C/min. During deposition of SnS nanostructures, the Ar flow rate was increased to 250 sccm. After 2 h, the furnace was allowed to cool naturally under constant Ar flow. The Au-coated Si substrate was removed from the furnace, which showed the presence of a grayish product uniformly covering the entire surface. This as-synthesized product was used for further characterization.

2.2. Characterization. The surface morphology of the as-synthesized SnS nanostructures was investigated by scanning electron microscopy (SEM, JEOL 6360A), and the elemental composition was obtained using an energy-dispersive X-ray spectrometer (EDAX). The phase identification of the as-synthesized product was obtained by X-ray diffraction (XRD, D8 Advance, Bruker AXS). The morphology and crystalline nature of the as-synthesized product were further studied by transmission electron microscopy (TEM, Tecnai G^2 20 Twin, FEI). For TEM studies, the SnS nanostructures were scratched off the substrate surface. The powdered material thus obtained was dispersed in analytical-grade acetone by ultrasonicating for 5 min. A drop of the ultrasonicated dispersion was put onto a carbon-coated copper grid for TEM analysis. The optical properties were investigated using an ultraviolet−visible−near infrared (UV−vis−NIR) spectrophotometer (model JASCO V-670). The photoluminescence (PL) spectrum was recorded at room temperature using a xenon lamp as an excitation source (PL spectrometer, Perkin-Elmer LS 55). The excitation wavelength was 500 nm. The chemical analysis of the as-synthesized SnS nanostructures was carried out using X-ray photoelectron spectroscopy (XPS, VG Microtech ESCA 3000).

The FE current density (J) versus applied electric field (E) and emission current (I) versus time (t) characteristics were measured in a planar "diode" configuration at a base pressure of ∼1.0×10^{-8} mbar. A typical "diode" configuration consisted of a phosphor-coated semi-transparent screen (a circular disc having a diameter of ∼40 mm) as an anode and SnS nanostructures deposited on the Au-coated Si substrate pasted on a stainless-steel holder (diameter of ∼4.5 mm) as a cathode. The FE measurements were carried out at a fixed cathode−anode separation of ∼1 mm. The emission current was measured on a Keithely electrometer (6514) by sweeping DC voltage applied to the cathode with a step of 40 V (0−40 kV, Spellman, Valhalla, NY). The details of vacuum processing and FE characteristics measurement are described elsewhere.[7] Special care was taken to avoid any leakage current using shielded cables and ensuring proper grounding. Before recording the FE measurements, preconditioning of the cathode was carried out by keeping it at ∼2000 V to remove loosely bound particles and/or contaminants by residual gas ion bombardment.

3. RESULTS AND DISCUSSION

3.1. Structural Studies. A typical XRD spectrum of an as-synthesized SnS nanostructure (Figure 1) exhibits a set of well-

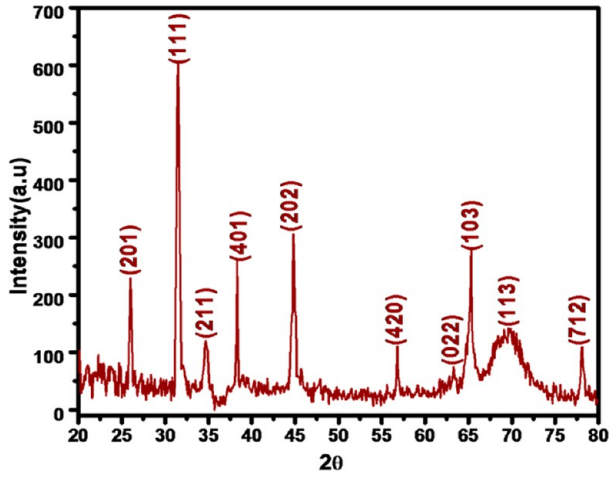

Figure 1. XRD pattern of the SnS nanowires synthesized at 800 °C.

defined diffraction peaks, implying the crystalline nature of the specimen. These peaks are indexed to the orthorhombic crystalline phase of SnS with lattice parameters: a, 11.186; b, 3.982; and c, 1.087 nm [Joint Committee on Powder Diffraction Standards (JCPDS) card, no. 73-1859]. Interestingly, the XRD pattern does not show diffraction peak(s) corresponding to other phases, such as SnS_2, Sn_2S_3, SnO, etc., indicating high purity of the as-synthesized product. Thus, the XRD analysis clearly reveals the formation of the high-purity crystalline SnS phase under the prevailing experimental conditions.

3.2. Surface Morphology. The surface morphology of the as-prepared SnS film on the Au-coated Si substrate was examined under SEM. The SEM images recorded at different magnifications (panels a−d of Figure 2) show the formation of randomly distributed nanowires. A careful observation of the SEM images reveals the formation of ultralong nanowires having a diameter in the range of 70−80 nm. The SEM image (Figure 2d) shows that some of the nanowires are protruding away from the substrate surface. Compositional analysis of the SnS nanowires was performed using an EDAX spectrum, which indicated the presence of Sn and S in the as-synthesized product (see Figure S1 of the Supporting Information). Interestingly, in the EDAX spectrum, no signatures because of oxygen were observed, which supports the formation of the SnS phase under the experimental conditions.

3.3. TEM Analysis. For structural analysis and understanding the crystallographic features of the as-synthesized product, TEM studies were carried out. Panels a and b of

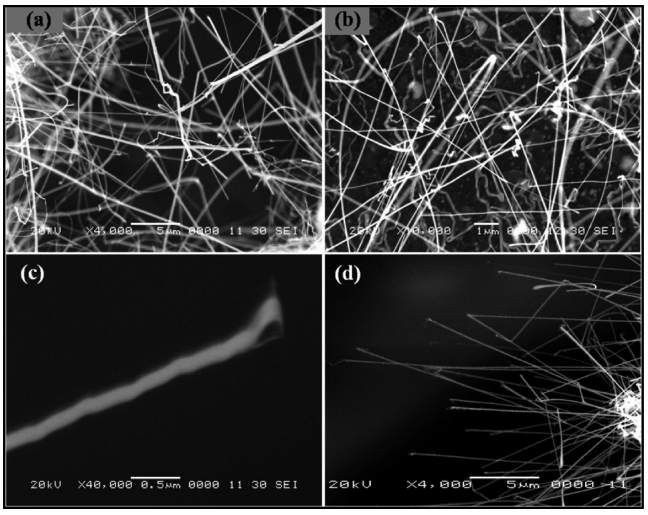

Figure 2. SEM images of the SnS nanowires deposited on the Au-coated Si substrate recorded at different magnifications: (a) 4000×, (b) 10000×, and (c) 40000×. (d) SEM image showing some of the SnS nanowires protruding away from the surface.

Figure 3 depict bright-field TEM images, showing the formation of randomly distributed SnS nanowires, with an

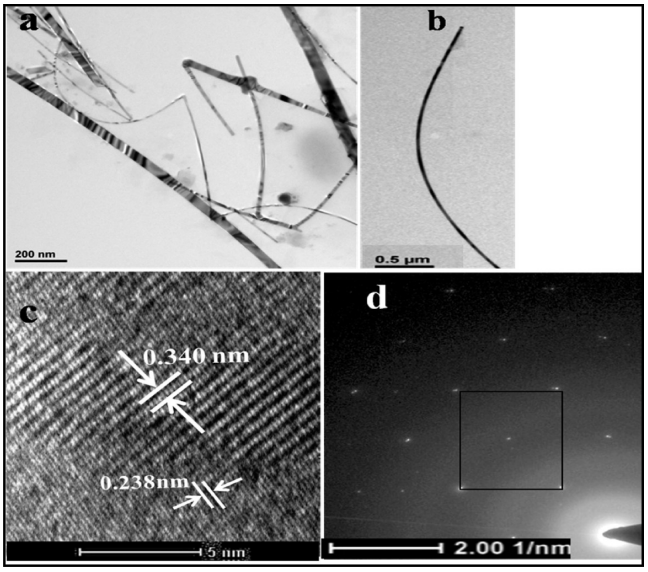

Figure 3. TEM images of (a) SnS nanowires and (b) single SnS nanowire, (c) high-resolution image of a single SnS nanowire, and (d) SAED pattern.

average diameter of 70 nm. The lattice-resolved high-resolution transmission electron microscopy (HRTEM) image of a single SnS nanowire (Figure 3c) clearly reveals its crystalline nature. Two distinct fringe patterns with "*d*" spacing of 0.23 and 0.34 Å are observed in the image, which correspond to the (111) and (201) lattice planes of the SnS orthorhombic phase, respectively. Furthermore, it is well-known that, in the layered structure of SnS, each tin atom is coordinated by six sulfurs in a highly distorted octahedral geometry. The distortion leads to three short and three long Sn−S bonds, having lengths of ∼2.7 and ∼3.4 Å, respectively.[14] The two lattice fringes observed in the HRTEM image may arise from the distorted octahedral geometry. The selected area electron diffraction (SAED) pattern, depicted in Figure 3d, confirms the single-crystalline nature of the SnS nanowires.

3.4. Optical Studies. To reveal the optical properties of the SnS nanowires, we have measured the UV−vis−NIR absorption in the range of 550−1400 nm (Figure 4a). The

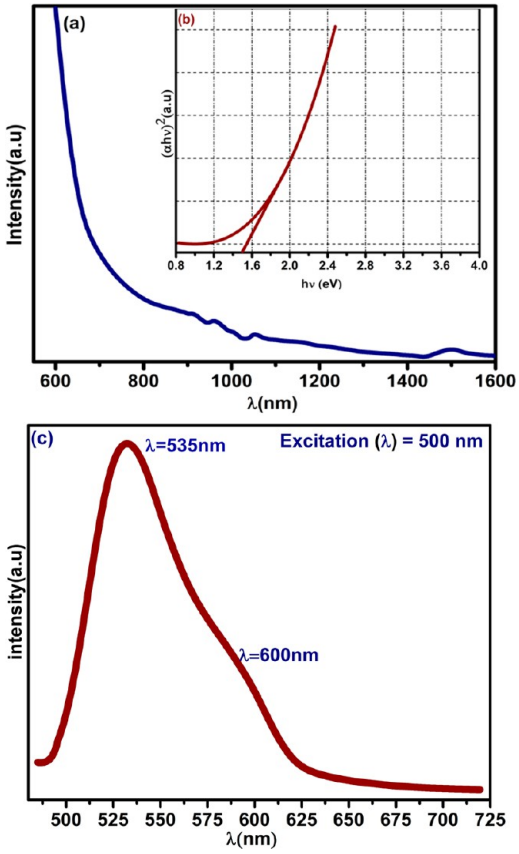

Figure 4. (a) Optical absorption spectrum of SnS nanowires. (b) Inset depicts a Tauc plot of ($h\nu$) versus $(\alpha h\nu)^2$ derived from observed optical data. (c) PL spectrum of deposited SnS nanowires recorded at room temperature.

spectrum exhibits high absorption in a short wavelength region, which decays rapidly with the increase in the wavelength, showing negligible absorption in the long wavelength region. The spectrum is observed to be identical to the earlier reports.[8] A careful observation of the spectrum shows the appearance of a shoulder around ∼900 nm, indicative of the excitation of electrons from the valence band maximum to the conduction band minimum. The band gap energy, estimated from a plot of $(\alpha h\nu)^2$ versus incident photon energy ($h\nu$) (inset of Figure 4a), is found to be ∼1.4 eV, which is slightly higher than the bulk value, ∼1.32 eV. The observed blue shift in the band gap energy with reference to bulk (microcrystalline) SnS powder is attributed to nanometric dimensions and defects present in the SnS nanowires (see Figure S3 of the Supporting Information).

3.5. PL. A typical room-temperature PL spectrum of the SnS nanowires recorded in the spectral range from 450 to 725 nm is shown in Figure 4c. The PL spectrum shows a broad emission peak centered at ∼535.3 nm (green emission), which can be ascribed to high-level transitions in SnS. In the PL spectra of SnS nanostructures and thin films, observation of peaks in the visible region has been reported in the literature.[15,16] Yei et al.

dx.doi.org/10.1021/am405039j | ACS Appl. Mater. Interfaces 2014, 6, 2018−2025

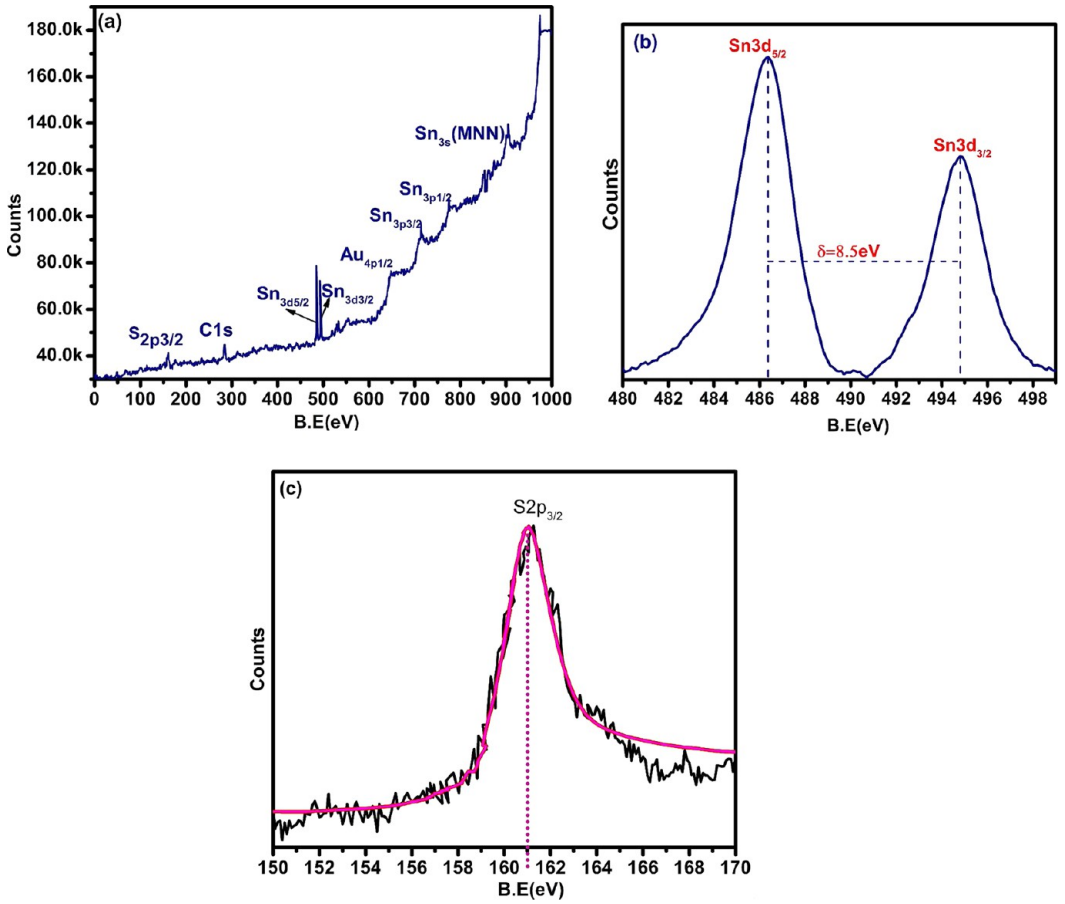

Figure 5. XPS spectra of the SnS nanowires: (a) survey scan, (b) Sn $3d_{5/2}$ and Sn $3d_{3/2}$ states, and (c) S $2p_{3/2}$ state.

have observed blue emission around 471 nm in the PL spectrum of SnS nanowires synthesized using a chemical vapor deposition (CVD) route. However, the authors have not explained the origin of this visible emission.[15] Furthermore, Devika et al. have observed signatures at ∼414, 550, and 530 nm in the PL spectrum of SnS thin films grown on amorphous and lattice matched crystalline substrates.[16] The authors have assigned these peaks to the presence of a high density of defects, such as sulfur and tin vacancies, interstitials, stacking faults, etc., in the SnS films. We believe that the origin of such high-level transitions in narrow band gap semiconductors, such as SnS, can be due to the Burstein−Moss effect in a semiconductor.[17] In the present case, the observed features of a broad peak at ∼535 nm and a shoulder around ∼600 nm may be attributed to the defects present in the SnS nanowires.

3.6. XPS Studies. Figure 5a depicts a survey scan of the XPS spectrum of as-synthesized SnS nanowires. The binding energy was corrected for specimen charging, through referencing C 1s to 284.6 eV. The XPS spectrum shows signatures of Sn and S only, implying purity of the specimen. The survey scan (Figure 5a) is further resolved in different parts corresponding to Sn and S energy levels. The Gaussian-fitted Sn 3d scan (Figure 5b) exhibits two well-defined peaks at 486.3 and 494.8 eV, which are ascribed to the Sn $3d_{5/2}$ and Sn $3d_{3/2}$ levels, resulting from the spin-orbit interaction in the metal sulfide, respectively. The energy gap between the Sn $3d_{5/2}$ and Sn $3d_{3/2}$ levels is found to be 8.5 eV. The observed Sn 3d spectrum is identical to those reported for various SnS nanostructures and films.[15,18] In addition to the Sn energy levels, a signature of the S $2p_{3/2}$ level is observed at 160.5 eV (Figure 5c).

A carful observation of the survey scan reveals the appearance of some peaks at ∼530, 650, and 850 eV. The low-intensity peak observed around ∼530 eV, a signature of the O $1s_{1/2}$ level, implies the presence of oxygen in the sample. Although XPS analysis is carried out under an ultrahigh vacuum (UHV) environment, some impurities, such as oxygen, can become incorporated into the sample, when exposed to the ambient environment. Because the sample was not subjected to any cleaning/degassing treatment prior to XPS analysis, the physisorbed oxygen present in the sample give rise to its characteristic signature in the XPS spectrum. The peak at ∼650 eV, observed in the XPS spectrum, is representative of the Au $4p_{1/2}$ level. It may be speculated that, in some of the SnS nanowires (not fully grown), Au particles might be present at their apex. The peak observed around 650 eV is attributed to the Au $4p_{1/2}$ energy level. The other peak observed at 850 eV represents the sub-binding energies of Sn, as described in the XPS handbook. Interestingly, no evidence of Sn^{4+} (binding energy at 485.5 eV) was observed in the spectrum. Thus, the XPS results clearly indicate the formation of the SnS phase under the prevailing experimental conditions.

3.7. Temperature-Dependent Morphological Evolution. To reveal the effect of the temperature on the morphology and, furthermore, to elucidate the growth mechanism of SnS nanowires, several experiments were carried out by varying the synthesis temperature in the range from 700 to 1000 °C, keeping the other process variables unaltered.

dx.doi.org/10.1021/am405039j | ACS Appl. Mater. Interfaces 2014, 6, 2018−2025

Scheme 1 depicts the SEM image of the SnS nanostructures synthesized at different temperatures. At 700 °C, the formation of irregular-shaped tiny particles/crystallites was observed. When the synthesis was carried out at 800 °C, very fine, ultralong randomly distributed nanowires were obtained. At 900 °C, the nanowires were observed to bunch together, and a further increase in the temperature to 1000 °C resulted in the formation of spherical aggregates. A careful observation of the SEM image reveals that these spherical aggregates are composed of the sheets made up of a random network of the nanowires.

Scheme 1. Schematic of the Temperature-Dependent Morphological Evolution of SnS Structures

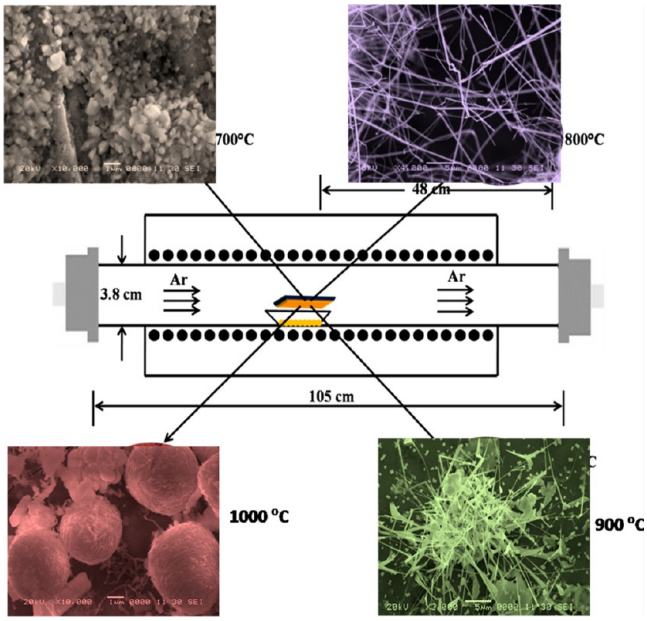

3.8. Growth Mechanism. To shed light on the growth mechanism of SnS nanowires, SEM analysis of the resultant products synthesized for different durations (15, 30, 45, 75, and 120 min) was carried out. On the basis of the SEM analysis, we herein propose a plausible growth mechanism of the SnS nanowires, depicted in Scheme 2. The Au-coated Si substrate exhibits granular morphology, and the Au particles are seen to cover the entire substrate surface (panel a of Scheme 2). When the deposition was carried out for 15 min, the formation of Au−Sn nanodroplets is observed (panel b of Scheme 2). The formation of the Au−Sn phase was confirmed from the XRD analysis (see Figure S2 of the Supporting Information). As the synthesis is carried out at 800 °C and the eutectic point of the Au−Sn phase is 380 °C, the formation of the Au−Sn droplets can be thermodynamically anticipated. Thus, after 15 min, the Au film exhibits thermally activated transformation, leading to the formation of Au−Sn nanodroplets. These Au−Sn nanodroplets act as energetically favored sites for adsorption of the incoming Sn and S vapors driven by the carrier gas (Ar). With gradual absorption of the Sn and S vapors, when the liquid droplets reach the supersaturation concentration, growth of a stable Sn−S phase is initiated via the vapor−liquid−solid (VLS) mechanism and the formation of small crystallites of SnS is observed for the 30 min duration case (panel c of Scheme 2).

When the synthesis was carried out for 45 min, the formation of 1D SnS nanostructures is observed (panel d of Scheme 2). The Au−Sn nuclei facilitate growth of the 1D structures via the VLS mechanism, in a manner similar to that observed for other semiconducting nanostructures, such as ZnS and ZnO.[19−21] The Au−Sn nuclei migrate to the top of the nanostructure as seen in the SEM images (panels c and d of Scheme 2). Owing to their high secondary electron emission yield, the Au−Sn nuclei appear "bright" in contrast to the SnS counterpart. Interestingly, we have also observed the presence of the Au−Sn droplet at the tip of the 1D SnS nanostructures in a low-magnification bright-field TEM image (panel a of Scheme 3). A further increase in the synthesis duration leads to an increase in the length of the SnS nanostructures with simultaneous reduction in their diameter. Finally, after a 2 h duration, the formation of ultralong and very fine SnS nanowires is observed. Interestingly, in the case of these ultralong SnS nanowires, the presence of the Au−Sn nuclei at the tip of the nanowires is not observed in the TEM images (panels b and c of Scheme 3). It may be speculated that, because of the ultralong nature of the

Scheme 2. Schematic of the VLS Growth Mechanism of SnS Nanowires

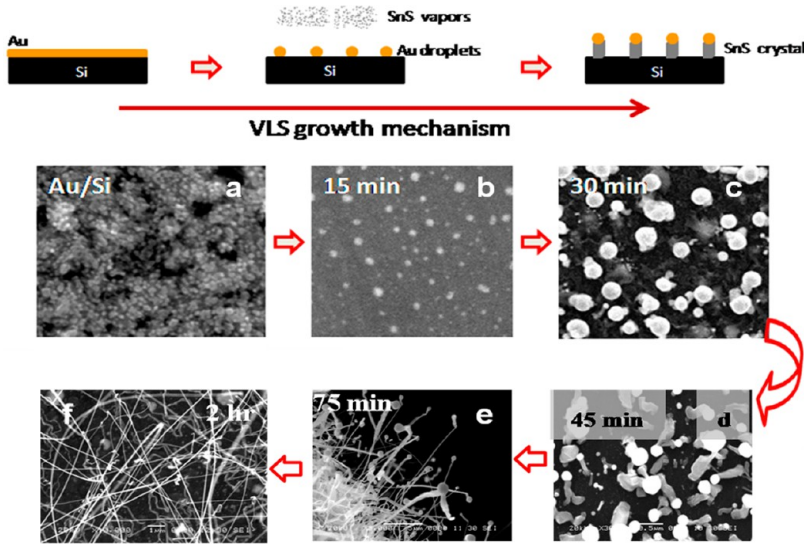

dx.doi.org/10.1021/am405039j | ACS Appl. Mater. Interfaces 2014, 6, 2018−2025

Scheme 3. Evolution of the SnS Nanowires as Per the Duration of Synthesis

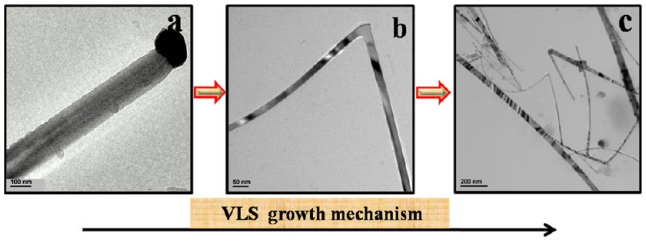

nanowires, the Au−Sn particles may become detached from the tip of the nanowires at some point of its growth.

The diameter of the Au−Sn droplet is one of the crucial parameters governing the overall growth of the nanostructures. Measurements over a large number of nanowires have revealed that, when the diameter of the droplet is equal to or smaller than the width of the nanowires, no bending occurs and straight nanowires are developed, whereas in the case of large size droplets, the nanowires exhibit the tendency to change the growth direction at an angle with respect to the initial growth axis. In the present studies, we have observed the formation of a few "L"-shaped nanowires.

From the viewpoint of growth kinetics, the VLS mechanism emphasizes that surface diffusion of reactant species and their preferential incorporation at high-surface-energy sites maintains the continuous growth of nanostructures.[21] The process can depict the intrinsic crystallography of materials into nanostructures to form well-faceted structures.[20] With Sn−S being a layered structure, during its growth, it has many dangling bonds at the two edges, which can easily incorporate atoms directly from the vapor phase or those diffusing from the bottom surface. Therefore, the vapor−solid (VS) growth also takes place in addition to the VLS process.[22] The low vapor pressure (order of 10^{-7} bar at 800 °C)[23] and low ionic mobility of Sn[24] ensure a slow and steady supply of source metal species that may favor the production of such fine nanostructures. The formation of L-shaped nanowires can be explained below. The larger Au−Sn droplets have a low surface-interfacial energy compared to the smaller droplets, and their shape is much more sensitive to perturbation during growth. Such perturbation can cause a change in the growth direction without increasing the free energy and can lead to the formation of "L" structures. The processes of forming "L"-shaped nanowires terminate in the second step, with the rest of the nanowires maintaining the diameter and growing as straight structures.

3.9. FE. The FE current density versus applied field (J−E) characteristic of the SnS nanowires is depicted in Figure 6a. As the applied voltage is gradually increased, the emission current is observed to increase very rapidly, indicating that the emission is indeed as per the Fowler−Nordheim (F−N) theory.[25] The values of the turn-on and threshold fields, defined as the fields required to draw emission current densities of ∼1 and ∼10 μA/cm^2, respectively, are found to be ∼1.65 and ∼1.98 V/μm, for an anode−cathode separation of ∼1 mm. Interestingly, a very high emission current density of ∼2.48 mA/cm^2 has been drawn from the emitter at a relatively lower applied electric field of ∼4.55 V/μm. The observed values of the turn-on and threshold fields are lower than those reported for various metal

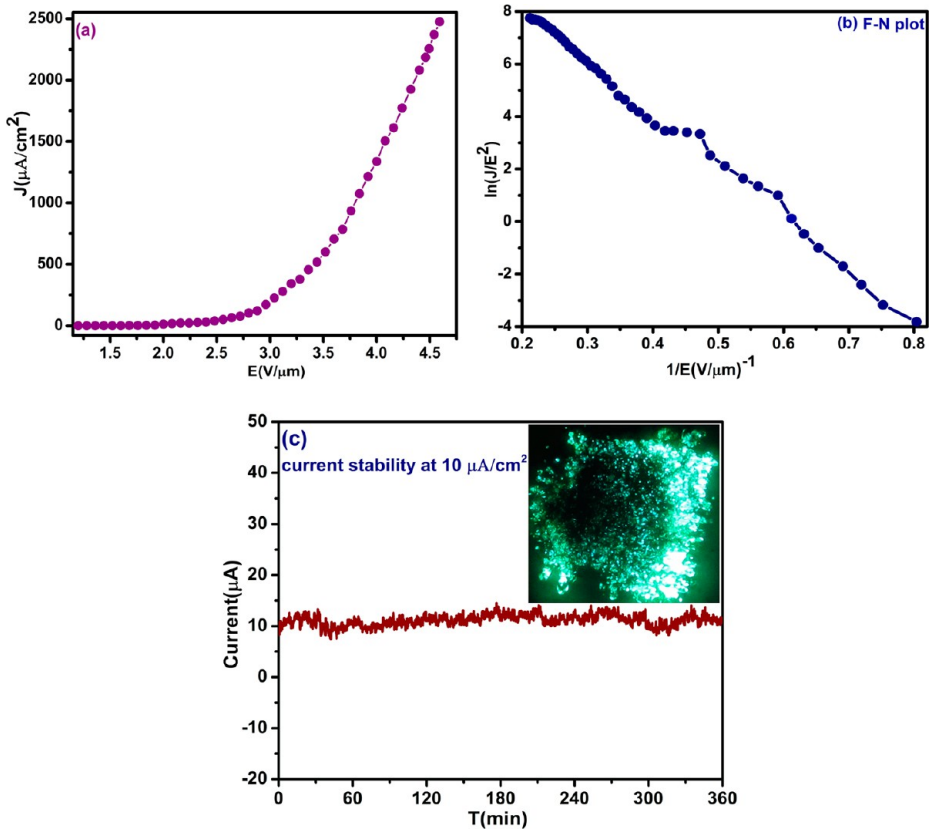

Figure 6. FE characteristics of the SnS nanowire emitter: (a) emission current density versus applied electric field (J−E) curve (b) F−N plot, and (c) emission current versus time (I−t) plot. The inset of panel c shows a typical FE image recorded at a current density of 10 μA/cm^2.

dx.doi.org/10.1021/am405039j | ACS Appl. Mater. Interfaces 2014, 6, 2018−2025

chalcogenide nanostructures (complied in Table 1). The lowest values of the turn-on and threshold fields are attributed to the high aspect ratio of the SnS nanowires, owing to their very fine diameter and ultralong nature. Furthermore, as seen from the SEM images, the areal density of the SnS nanowires is seen to be moderate, offering less of a field screening effect. The extraction of a very high current density (~2.48 mA/cm^2) at a relatively lower applied field (~4.55 V/μm) in comparison to other chalcogenide nanostructures can be attributed to its low band gap value (1.40 eV) compared to SnO_2 (3.40 eV) and ZnS (3.75 eV). In the case of semiconducting field emitters, it is believed that the emission current is composed of tunneling of charge carriers from both the conduction band and valence band.[26,27] Initially, at a lower applied field strength, the emission is mainly due to tunneling of charge carriers from the conduction band, and when the applied field strength becomes enough (for effective bending of the potential barrier at the valence band maximum), the charge carriers from the valence band start tunneling, thereby contributing to the observed emission current. Therefore, conceptually, because the effective work function of SnS (defined with reference to the valence band maximum) is smaller than that of other chalcogenides (SnO_2, and ZnS), the valence band charge carriers will exhibit tunneling probability at a relatively lower applied field strength. Thus, the observed superior values of turn-on and threshold fields and extraction of a high emission current density at a lower applied electric field are attributed to the synergic effect of a high aspect ratio, smaller areal density, less screening effect, and narrow band gap of the SnS nanostructures.

Table 1. Turn-on Field Values of SnS Nanowires and Various Metal Chalcogenide Nanostructures Reported in the Literature

number	morphology	turn-on field (V/μm)	threshold field (V/μm)	reference
1	Bi_2S_3 nanowires	0.1 μA/cm^2 at 2.08	50 μA/cm^2 at 3.36	31
2	GaS nanobelts	0.1 nA/cm^2 at 2.9	5.7 μA/cm^2 at 6.0	29
3	ZnS nanotubes	10 μA/cm^2 at 5.43	11 mA/cm^2 at 7.45	32
4	CdS nanowires	0.1 μA/cm^2 at 0.26	14.6 μA/cm^2 at 0.65	33
5	SnS nanowires	1 μA/cm^2 at 1.65	10 μA/cm^2 at 1.98	present work

The modified form of the F–N equation[28] for a flat multi-tip emitter (comprised of an assembly of a large number of nanostructures deposited in thin-film form on a suitable substrate) is given as

$$J = \lambda_m a\phi^{-1}E^2\beta^2 \exp\left(-\frac{b\phi^{3/2}}{\beta E}\nu_F\right) \quad (1)$$

where J is the emission current density, E is the applied average electric field, a and b are constants, typically 1.54×10^{-10} (A V^{-2} eV) and 6.83×10^3 (V eV$^{-3/2}$ μm^{-1}), respectively, φ is the work function of the emitter material, λ_m is a macroscopic pre-exponential correction factor, υ_F is the value of the principal Schottky–Nordheim barrier function (a correction factor), and β is the field enhancement factor. In the present studies, the applied electric field E is defined as $E = V/d$, where V is the applied voltage and d is the separation between the anode and cathode (~1 mm). Furthermore, the emission current density J is estimated as $J = I/A$, where I is the observed value of the emission current and A is the total area of the emitter (~1 cm^2).

The J–E characteristic is further analyzed by plotting a graph of $\ln(J/E^2)$ versus $(1/E)$, known as a F–N plot. The observed F–N plot (Figure 6b) exhibits overall nonlinear behavior indicative of the semiconducting nature of the emitter. Such nonlinear F–N plots have been reported for various semiconducting nanostructure emitters.[29,30] Usually, the slope of the F–N plot is used to estimate the value of the field enhancement factor (β). However, it has been observed that, for a flat multi-tip emitter, this procedure leads to overestimation of the β value, which predicts the presence of an unphysical local electric field ($E_{local} = \beta E_{average}$)[25] at the emitting site. Hence, in the present studies, we have not estimated the value of the field enhancement factor β.

The emission current versus time (I–t) plot corresponding to the preset value of ~10 μA, recorded over a period of 6 h (with a sampling interval of 10 s) at a base pressure of 1×10^{-8} mbar, is depicted in Figure 6c. The emission current exhibits small excursions along with "spike"-type fluctuations superimposed on the base level. The appearance of "spike"-type fluctuations in the emission current is attributed to field-induced adsorption, desorption, and/or migration of the residual gas molecules. These processes occurring on the atomic scale lead to an instantaneous change in the "local" work function at the emission site, thereby generating a "spike" in the emission current. The average emission current is seen to remain fairly stable over the entire duration, which indicates good physical and chemical stability of the emitter. The FE image recorded at the inset of the current stability studies (inset of Figure 6c) shows a number of bright spots, confirming that the emission is indeed from the most protruding SnS nanowires. The overall superior FE characteristics suggest the SnS nanowire field emitter as a promising electron source for practical applications in various vacuum micro/nanoelectronic devices.

4. CONCLUSION

Synthesis of single-crystalline SnS nanowires on Au-coated Si substrate has been achieved by a facile thermal evaporation route under optimized process variables. The XRD and XPS analyses reveal the formation of a pure orthorhombic phase of SnS under the optimized conditions. The FE characteristics of the SnS nanowire emitter in terms of turn-on and threshold field values are found to be superior to those reported for other chalcogenide nanostructures. Furthermore, a high emission current density of ~2.48 mA/cm^2 could be drawn from the emitter at a relatively lower applied field of ~4.55 V/μm. The SnS nanowire emitter exhibits a fairly stable emission at a preset value of ~10 μA over a long-term duration of 6 h. The overall superior FE characteristics propose the SnS nanowire field emitter as a promising electron source for practical applications in various vacuum micro/nanoelectronic devices.

■ ASSOCIATED CONTENT

Supporting Information

EDAX studies (Figure S1), XRD spectrum (Figure S2), and UV–vis spectroscopy of bulk SnS (Figure S3). This material is available free of charge via the Internet at http://pubs.acs.org.

AUTHOR INFORMATION

Corresponding Author

*Telephone: 020-25692678, ext. 310. Fax: 020-25691684. E-mail: mam@physics.unipune.ac.in.

Notes

The authors declare no competing financial interest.

ACKNOWLEDGMENTS

Sachin R. Suryawanshi gratefully acknowledges the financial support from Bhabha Atomic Research Centre (BARC), Mumbai, India, for the award of Junior Research Fellowship under BARC−University of Pune (UoP) memorandum. Mahendra A. More thanks the Board of College and University Development (BCUD), University of Pune, Pune, India, for the financial support provided for the synthesis and FE work under CNQS-UPE-UGC program activity. The authors also thank Dr. Satishchandra B. Ogale (NCL, Pune, India) for his valuable guidance in SnS_2 synthesis and HRTEM analysis. The authors also thank Prof. S. K. Date for valuable discussion on the XPS results.

REFERENCES

(1) Suresh, S. *Appl. Nanosci.* **2013**, 1−5.
(2) Santos Cruz, J.; Mayén Hernández, S. A.; Paraguay Delgado, F.; Zelaya Angel, O.; Castanedo Pérez, R.; Torres Delgado, G. *Int. J. Photoenergy* **2013**, *2013*, 1−9.
(3) Moreels, I.; Lambert, K.; Smeets, D.; De Muynck, D.; Nollet, T.; Martins, J. C.; Vanhaecke, F.; Vantomme, A.; Delerue, C.; Allan, G.; Hens, Z. *ACS Nano* **2009**, *3*, 3023−3030.
(4) Barrelet, C. J.; Greytak, A. B.; Lieber, C. M. *Nano Lett.* **2004**, *4*, 1981−1985.
(5) Chen, Z. G.; Cheng, L.; Xu, H. Y.; Liu, J. Z.; Zou, J.; Sekiguchi, T.; Lu, G. Q.; Cheng, H. M. *Adv Mater.* **2010**, *22*, 2376−2380.
(6) Shinde, D. R.; Chavan, P. G.; Sen, S.; Joag, D. S.; More, M. A.; Gadkari, S. C.; Gupta, S. K. *ACS Appl. Mater. Interfaces* **2011**, *3*, 4730−4735.
(7) Sinha, G.; Panda, S. K.; Datta, A.; Chavan, P. G.; Shinde, D. R.; More, M. A.; Joag, D. S.; Patra, A. *ACS Appl. Mater. Interfaces* **2011**, *3*, 2130−2135.
(8) Yue, G. H.; Wang, L. S.; Wang, X.; Chen, Y. Z.; Peng, D. L. *Nanoscale Res. Lett.* **2009**, *4*, 359−363.
(9) Ghazali, A.; Zainal, Z.; Zobir Hussein, M.; Kassim, A. *Sol. Energy Mater. Sol. Cells* **1998**, *55*, 237−249.
(10) Deng, Z.; Cao, D.; He, J.; Lin, S.; Lindsay, S. M.; Liu, Y. *ACS Nano* **2012**, *6*, 6197−6207.
(11) Lu, J.; Nan, C.; Li, L.; Peng, Q.; Li, Y. *Nano Res.* **2012**, *6*, 55−64.
(12) Radovsky, G.; Popovitz-Biro, R.; Staiger, M.; Gartsman, K.; Thomsen, C.; Lorenz, T.; Seifert, G.; Tenne, R. *Angew. Chem., Int. Ed. Engl.* **2011**, *50*, 12316−12320.
(13) Chao, J.; Xie, Z.; Duan, X.; Dong, Y.; Wang, Z.; Xu, J.; Liang, B.; Shan, B.; Ye, J.; Chen, D.; Shen, G. *CrystEngComm* **2012**, *14*, 3163.
(14) Jiang, T.; Ozin, G. A. *J. Mater. Chem.* **1998**, *8*, 1099−1108.
(15) Yue, G. H.; Lin, Y. D.; Wen, X.; Wang, L. S.; Chen, Y. Z.; Peng, D. L. *Appl. Phys. A: Mater. Sci. Process.* **2011**, *106*, 87−91.
(16) Devika, M.; Koteeswara Reddy, N.; Prashantha, M.; Ramesh, K.; Venkatramana Reddy, S.; Hahn, Y. B.; Gunasekhar, K. R. *Phys. Status Solidi A* **2010**, *207*, 1864−1869.
(17) Grundmann, M. *The Physics of Semiconductors: An Introduction Including Devices and Nanophysics*; Springer: New York, 2006.
(18) Price, L. S.; Parkin, I. P.; Hardy, A. M. E.; Clark, R. J. H.; Hibbert, T. G.; Molloy, K. C. *Chem. Mater.* **1999**, *11*, 1792−1799.
(19) Ye, C.; Fang, X.; Hao, Y.; Teng, X.; Zhang, L. *J. Phys. Chem. B* **2005**, *109*, 19758−19765.
(20) Pan, Z. W.; Dai, Z. R.; Wang, Z. L. *Science* **2001**, *291*, 1947−1949.
(21) Hao, Y.; Meng, G.; Wang, Z. L.; Ye, C.; Zhang, L. *Nano Lett.* **2006**, *6*, 1650−1655.
(22) Peng, H.; Meister, S.; Chan, C. K.; Zhang, X. F.; Cui, Y. *Nano Lett.* **2007**, *7*, 199−203.
(23) Geiger, F.; Busse, C. A.; Loehrke, R. I. *Int. J. Thermophys.* **1987**, *8*, 425−436.
(24) Knudsen, N. *Solid State Ionics* **1989**, *35*, 51−55.
(25) Forbes, R. G. *J. Vac. Sci. Technol., B: Microelectron. Nanometer Struct.—Process., Meas., Phenom.* **1999**, *17*, 526.
(26) Al-Tabbakh, A. A.; More, M. A.; Joag, D. S.; Ramgir, N. S.; Mulla, I. S.; Pillai, V. K. *Appl. Phys. Lett.* **2007**, *90*, 162102.
(27) Al-Tabbakh, A. A.; More, M. A.; Joag, D. S.; Mulla, I. S.; Pillai, V. K. *ACS Nano* **2010**, *4*, 5585−5590.
(28) Kashid, R. V.; Late, D. J.; Chou, S. S.; Huang, Y. K.; De, M.; Joag, D. S.; More, M. A.; Dravid, V. P. *Small* **2013**, *9*, 2730−2734.
(29) Panda, S. K.; Datta, A.; Sinha, G.; Chaudhuri, S.; Chavan, P. G.; Patil, S. S.; More, M. A.; Joag, D. S. *J. Phys. Chem. C* **2008**, *112*, 6240−6244.
(30) Navale, S. C.; Sheini, F. J.; Patil, S. S.; Mulla, I. S.; Joag, D. S.; More, M. A.; Gosavi, S. W. *J. Nano Res.* **2009**, *5*, 231−237.
(31) Warule, S. S.; Chaudhari, N. S.; Kale, B. B.; Pandiraj, S.; Khare, R. T.; More, M. A. *CrystEngComm* **2013**, *15*, 890.
(32) Gautam, U. K.; Fang, X.; Bando, Y.; Zhan, J.; Golberg, D. *ACS Nano* **2008**, *2*, 1015−1021.
(33) Chavan, P. G.; Badadhe, S. S.; Mulla, I. S.; More, M. A.; Joag, D. S. *Nanoscale* **2011**, *3*, 1078−1083.